



High-efficiency low-noise optomechanical crystal photon-phonon transducers

SAMEER SONAR,^{1,2,†}  UTKU HATİPOĞLU,^{1,2,†}  SRUJAN MEESALA,^{1,2} DAVID P. LAKE,^{1,2}
HENGJIANG REN,^{1,2,3} AND OSKAR PAINTER^{1,2,4,*} 

¹Institute for Quantum Information and Matter, California Institute of Technology, Pasadena, California 91125, USA

²Kavli Nanoscience Institute and Thomas J. Watson, Sr., Laboratory of Applied Physics, California Institute of Technology, Pasadena, California 91125, USA

³Current address: Anyon Computing Inc., Emeryville, California 94608, USA

⁴AWS Center for Quantum Computing, Pasadena, California 91125, USA

[†]These authors contributed equally to this work.

*opainter@caltech.edu

Received 9 August 2024; revised 30 November 2024; accepted 1 December 2024; published 17 January 2025

Optomechanical crystals (OMCs) enable coherent interactions between optical photons and microwave acoustic phonons, and represent a platform for implementing quantum transduction between microwave and optical signals. Optical-absorption-induced thermal noise at cryogenic (millikelvin) temperatures is one of the primary limitations of performance for OMC-based quantum transducers. Here, we address this challenge with a two-dimensional silicon OMC resonator that is side-coupled to a mechanically detached optical waveguide, realizing a six-fold reduction in the heating rate of the acoustic resonator compared to prior state-of-the-art, while operating in a regime of high optomechanical-backaction and millikelvin base temperature. This reduced heating translates into a demonstrated phonon-to-photon conversion efficiency of $93.1 \pm 0.8\%$ at an added noise of 0.25 ± 0.01 quanta, representing a significant advance toward quantum-limited microwave-optical frequency conversion and optically controlled quantum acoustic memories. © 2025 Optica Publishing Group under the terms of the [Optica Open Access Publishing Agreement](#)

<https://doi.org/10.1364/OPTICA.538557>

1. INTRODUCTION

Optomechanical crystals (OMCs) are periodic dielectric structures engineered to co-localize light and acoustic vibrations on the wavelength scale [1]. OMCs in one-dimensional silicon nanobeams have been used to demonstrate MHz-scale interaction rates between single photons and phonons confined in telecom-wavelength optical and GHz-frequency acoustic modes, respectively [2]. In recent years, these devices have enabled advances in quantum acoustics [3,4], and microwave-optical quantum transduction [5–8]. In these applications, OMCs are operated at temperatures ≤ 0.1 K to ensure negligible thermal occupation in GHz frequency acoustic modes. However, optical excitation of OMCs in this temperature regime is accompanied by local heating due to weak parasitic absorption of laser light. This effect results in elevated thermal occupation and reduced coherence of the acoustic mode [3,9], and limits the performance of OMCs as quantum memories and transducers. For instance, in the context of microwave-optical quantum transduction, operation of OMCs in the quantum coherent regime is currently possible in pulsed mode with reduced laser power, albeit at the expense of reduced efficiency for the optomechanical scattering process, and ultimately, a reduced entanglement generation rate for quantum networking applications [5,6].

Two-dimensional (2D) device geometries [10–13], which offer increased thermal contact with the substrate, are a promising approach to mitigate the detrimental effects of optical-absorption-induced heating in OMCs at millikelvin temperatures. These structures rely on a phononic bandgap to protect the acoustic mode of interest from clamping losses while leveraging a larger density of states at frequencies above the gap to allow high-frequency thermal phonons to escape out of the OMC cavity. However, a large thermal contact area can also lead to a significant influx of thermal phonons from sites of optical absorption external to the cavity. Such a phenomenon was noted in our prior work on 2D-OMCs in Ref. [11], where optical absorption in the coupling waveguide was found to be the dominant source of thermal noise in the acoustic mode. In principle, thermal isolation of the OMC cavity from the coupling optical waveguide could be achieved through mechanical detachment of both structures from one another while maintaining evanescent optical coupling. However, these requirements are challenging to engineer in a 2D geometry since abrupt termination of the OMC can result in significantly increased optical loss via parasitic edge modes. In this work, we overcome this challenge with a 2D-OMC with a novel side-coupled waveguide design and demonstrate a significant improvement in phonon-to-photon conversion performance over previous state-of-the-art [11]. We observe a six-fold reduction in the heating rate of the acoustic

resonator in the regime of high optomechanical backaction and millikelvin base temperatures. Under continuous-wave (pulsed) optical excitation, we show through optomechanical sideband thermometry that the device can perform phonon-to-photon conversion with an internal efficiency of $98.6 \pm 0.2\%$ ($93.1 \pm 0.8\%$) and an added noise of 0.28 ± 0.01 quanta (0.25 ± 0.01 quanta) at the highest optical powers used in our experiments. Our results indicate that side-coupled 2D-OMCs can enable high-fidelity quantum-coherent operations with acoustic modes and advance the performance of optomechanical quantum transducers and memories.

2. DESIGN OF THE SIDE-COUPLED 2D-OMC CAVITY

The OMC cavity in this work is designed on a 220 nm thick silicon device layer of a silicon-on-insulator (SOI) substrate. Figure 1(a) shows a helium ion microscope image of a fabricated device. The insets show (from left to right) unitcells of a snowflake, fish-bone waveguide, coupling waveguide, and the photonic crystal mirror. The snowflake crystal provides a pseudo-bandgap for TE-like optical guided waves and a full bandgap for all acoustic mode polarizations, whereas the fish-bone structure is engineered to maximize the combined photoelastic and moving boundary contributions to the optomechanical coupling. The coupling waveguide is designed with a half-snowflake unitcell to evanescently couple to the optical mode of the OMC cavity. The detailed design process and mode analysis underlying this configuration are presented in Supplement 1, Section 6. The gap between the two structures can be controlled to set the external coupling rate of the optical cavity. To facilitate measurements of the OMC in reflection, the coupling waveguide is terminated with a photonic crystal mirror. The orange inset on the right shows the supercell for the combined setup with the cavity and coupling waveguide. The corresponding optical bandstructure is shown in Fig. 1(b). The shaded region represents the relevant optical bandgap. The cavity (waveguide) band of interest is shown in solid red (blue). The corresponding electric field profile for cavity (waveguide) mode is shown on the right labeled 1 (2).

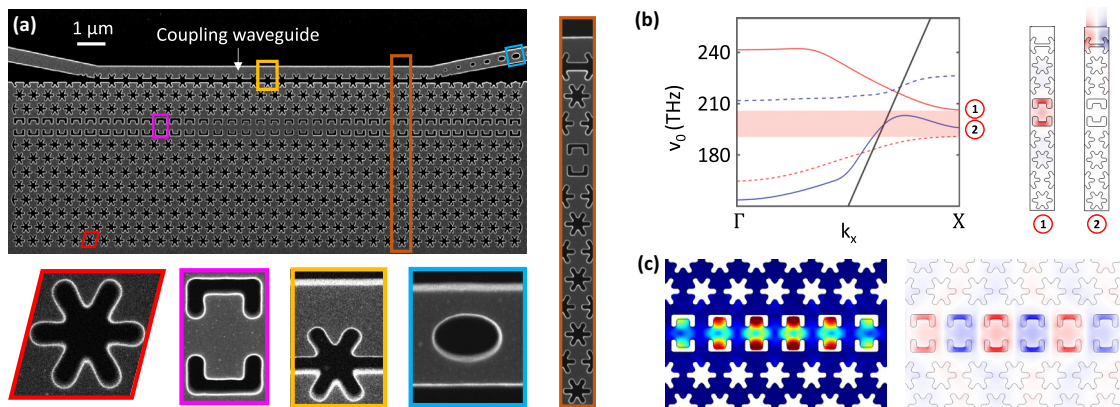


Fig. 1. Side-coupled 2D optomechanical crystal (OMC) cavity. (a) Helium-ion microscope image of a representative device with insets indicating salient features from left to right: unitcells of the 2D snowflake lattice, central fish-bone waveguide, optical coupling waveguide, and the optical waveguide mirror. The orange inset on the right shows the supercell of the geometry used to simulate optical and acoustic bandstructures. (b) Simulated optical bandstructure of the supercell. The solid red (blue) band has energy predominantly in the cavity (coupling waveguide). Transverse electric field profiles of these optical modes at the X-point are shown on the right. Dashed lines in the bandstructure indicate other guided modes. (c) FEM simulations of the acoustic (left; total displacement) and optical (right; transverse electric field) modes of the 2D-OMC cavity with acoustic resonance frequency, $\Omega_m/2\pi = 10.3$ GHz, and optical resonance wavelength, $\lambda = 1550$ nm, respectively.

Figure 1(c) illustrates the simulated acoustic breathing mode with a frequency of 10.3 GHz, and the transverse electric field distribution of the fundamental optical mode with a wavelength of 1550 nm. The energy of the optical mode is predominantly localized in the air gaps of the fish-bone structure to enhance optomechanical coupling due to the moving boundaries. For an air gap size of 70 nm, this design provides a vacuum optomechanical coupling rate, $g_{OM}/2\pi = 1.1$ MHz, in simulation. In principle, fabrication of smaller gaps (e.g., 20 nm) can allow for $g_{OM}/2\pi$ up to 2.5 MHz. More details are provided in Supplement 1, Section 7.

The devices are patterned using electron beam lithography and reactive ion etching, and are suspended by etching the underlying buried oxide layer with hydrofluoric acid etch. We present here the characterization of two devices, which we refer to as device I and II in our discussion. All measurements are performed in a dilution refrigerator, with the samples mounted to the mixing chamber plate at a temperature of $T_f \approx 10$ mK. The optical and acoustic mode parameters of both devices are tabulated in Supplement 1, Section 1. The primary difference between the two devices is their coupling to the external chip environment. For device I, the intrinsic acoustic damping rate, $\gamma_0/2\pi$, is measured to be 21.46 kHz, whereas device II is better isolated from the chip environment with a $\gamma_0/2\pi = 0.97$ kHz. We attribute the difference in $\gamma_0/2\pi$ between the two devices to a difference in the as-fabricated feature sizes. The effectiveness of the snowflake acoustic bandgap in suppressing acoustic radiation from the central cavity region depends on the frequency alignment of the localized mode and the acoustic bandgap, and is highly sensitive to the feature size and shape. A scanning electron microscope image of device I indicates that the patterned features are slightly more rounded and extended than the ideal design, whereas device II replicates the design more faithfully. Although unintentional, these as-fabricated differences in the two devices provide further information about how they thermalize with their environment.

3. OPTICAL-ABSORPTION-INDUCED HOT BATH

Previous measurements on OMC devices in the dilution refrigerator have shown that the acoustic mode thermalizes to temperatures

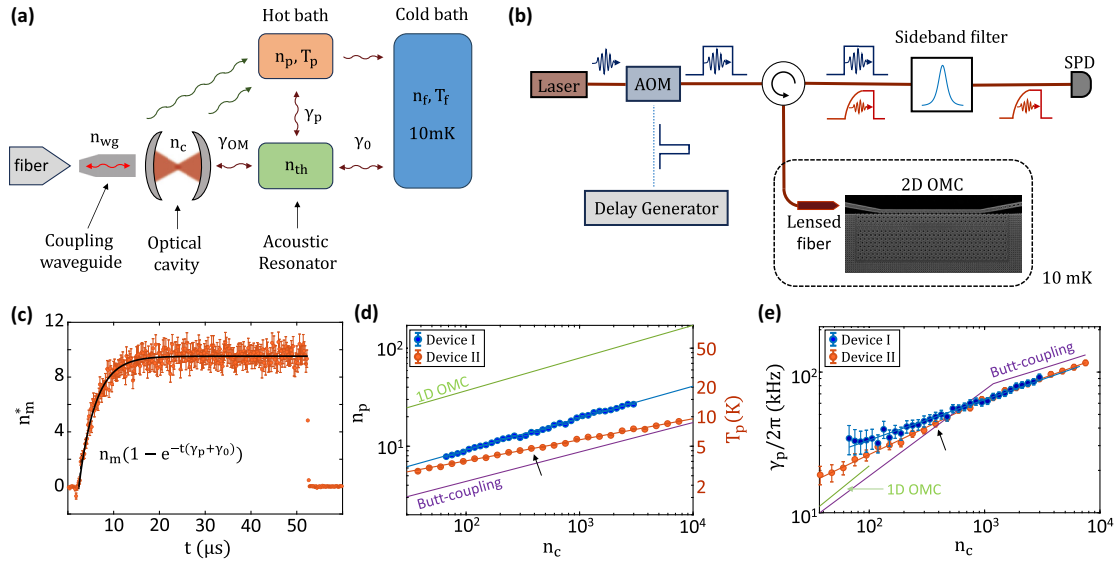


Fig. 2. Characterization of optical-absorption-induced hot bath. (a) Schematic showing interactions of the acoustic resonator with various baths considered in our heating model. (b) Schematic of measurement setup for time-resolved measurements of the hot bath using single-photon counting on the optical sideband generated by thermal motion of the acoustic resonator. (c) Measurement of the transient thermal occupation of the acoustic resonator, n_m^* , in response to a rectangular optical pulse on resonance with the optical cavity (pulse duration $\tau_d = 50 \mu\text{s}$, repetition rate, $R = 1 \text{ kHz}$, and peak intracavity photon occupation, $n_c = 385$). The black line represents an exponential fit to the observed data with the characteristic rate, $\gamma_p + \gamma_0$, and steady-state thermal occupation, n_m . Here γ_0 is the intrinsic damping rate of the acoustic resonator and γ_p is the coupling rate to the optical-absorption-induced hot bath. (d) Thermal occupation of the hot bath, n_p estimated from measurements of n_m performed at varying optical power, shown on the x -axis in units of peak intra-cavity photon occupation, n_c . For comparison, n_p curves for 1D-OMC [3], butt-coupled 2D-OMC [11] are shown. (e) Variation of $\gamma_p/2\pi$ with n_c . The data point marked with an arrow in (d) and (e) corresponds to the data in (c) for $n_c = 385$.

well below 100 mK [3]. In our study, we model this connection to the cold substrate by a coupling to a cold bath with occupancy n_f ($< 10^{-3}$), at an intrinsic acoustic damping rate, γ_0 , as shown in Fig. 2(a). Under excitation with laser fields, optical-absorption-induced heating from the optical cavity and coupling waveguide is modeled by considering a hot bath at a thermal occupation, n_p (corresponding to a bath temperature, T_p), coupled to the acoustic mode at a rate γ_p . The acoustic resonator experiences optomechanical backaction at a rate γ_{OM} . We operate our devices in a low-power optical regime where radiation pressure shot noise is negligible. When the laser is tuned to the red motional sideband of the optical cavity (detuning $\Delta = -\Omega_m$), a parametric beamsplitter interaction allows us to operate the device as a linear, bi-directional converter between quantum states in the acoustic and optical modes at a rate $\gamma_{OM} = 4g_{OM}^2 n_c / \kappa_t$, where n_c is the intracavity photon occupation and κ_t is the total linewidth of the optical resonance [14].

As a first step towards characterizing the optical-absorption-induced hot bath we operate the laser on resonance with the optical cavity ($\Delta = 0$). Under this detuning condition the electric field amplitude in the waveguide is negligible compared to the cavity, and the optomechanical backaction rate is zero. This enables us to isolate optical absorption within the cavity alone without the effects of heating due to optical absorption in the waveguide or cooling due to optomechanical backaction. We measure the heating dynamics of the acoustic mode by detecting optical photons scattered from the laser field onto a motional sideband of the optomechanical cavity. In steady state, the occupation of the acoustic mode, n_m , is expected to be an average of the thermal occupations of the hot and the cold baths, weighted by the coupling rates of the acoustic mode to the respective baths, as given by the relation

$$n_m = \frac{\gamma_p n_p + \gamma_0 n_f}{\gamma_p + \gamma_0}. \quad (1)$$

Figure 2(b) shows the schematic of the measurement setup for n_m . We send laser pulses with pulse duration $\tau_d = 50 \mu\text{s}$ at a repetition rate $R = 1 \text{ kHz}$ to the device in the dilution refrigerator via a circulator. The optical signal reflected from the device is directed to a Fabry–Perot filter setup that suppresses the pump pulses and transmits photons generated on the motional sideband of the optomechanical cavity to a superconducting nanowire single-photon detector. Figure 2(c) shows the time-dependent occupation of the acoustic mode measured from heating induced by a square laser pulse with a peak power corresponding to $n_c = 385$. The rate of increase in the occupation is used to infer $\gamma_p + \gamma_0$, whereas the steady state occupation is used to infer n_m . Finally, the value of γ_0 is measured independently from ringdown measurements [3], thereby allowing us to extract the parameters γ_p and n_p of the hot bath from Eq. (1).

Figure 2(d) shows n_p as a function of n_c for devices I and II along with results from similar measurements performed previously on 1D-OMCs [3], and butt-coupled 2D-OMCs [11]. The vertical axis on the right represents the corresponding bath temperature T_p . The solid lines around the experimental data points for devices I and II are fits to the power law $n_p = An_c^k$. We find that the fits to the hot bath occupancies for devices I and II are $2.2 \times n_c^{0.31}$ and $2.9 \times n_c^{0.21}$, respectively. For comparison, we have also shown the fits to $n_p(n_c)$ for previously measured butt-coupled 2D-OMC (purple solid line) and 1D-OMC (green solid line) devices, corresponding to $1.1 \times n_c^{0.3}$ and $7.94 \times n_c^{0.33}$, respectively. As expected, the thermal conductance seems to be highest for the butt-coupled 2D-OMC, slightly lower for the side-coupled 2D-OMC devices that are restricted to approximately the half-plane, and lowest

for the 1D-OMCs. Of note, the power law of the side-coupled device II of this work ($k = 0.21$) deviates from other measured 1D and 2D-OMCs, and does not seem to follow from the simple phonon-bottleneck model of Ref. [3]. This suggests there may be more to the underlying conductance of heat from these structures. While a systematic study of this effect is beyond the scope of this article, we note that previous studies on phononic crystal structures have observed varying power laws for thermal conductance [15], and disorder-dependent thermal conductance [16,17], which may offer insights into the observed n_p power laws in this work.

Figure 2(e) shows the variation of γ_p with n_c . For device II, we find the power-law $\gamma_p/2\pi = 4.3$ (kHz) $\times n_c^{0.39}$ when $n_c < 1000$ and $\gamma_p/2\pi = 8.25$ (kHz) $\times n_c^{0.29}$ when $n_c > 1000$. The power-law exponent of 0.39 in the regime of low optical power is significantly different from 0.6 and 0.66 observed previously for butt-coupled 2D-OMC and 1D-OMC devices, respectively. This reduction can be explained by the reduced n_p power exponent of 0.21, together with a two-dimensional phonon bath (see Supplement 1, Section 10). For device I, in the regime of high optical power with $n_c > 1000$, $\gamma_p/2\pi = 8.7$ (kHz) $\times n_c^{0.29}$. For $n_c < 1000$, the measurement error on γ_p for device I is larger due to a higher intrinsic damping rate, γ_0 , thereby reducing the reliability of a fit in this regime. We observe that the power-law exponent for γ_p in the regime of high optical power is identical for devices I and II in this study, and also in close agreement with the butt-coupling geometry.

4. PHONON-TO-PHOTON TRANSDUCTION UNDER CONTINUOUS-WAVE LASER EXCITATION

After characterizing the optical-absorption-induced hot bath, we test the device with the laser tuned to the red motional sideband of the optical cavity ($\Delta = -\Omega_m$), relevant for phonon-photon transduction. The thermal occupation of the acoustic mode, n_{th} , due to optical-absorption-induced heating adds finite noise to any transduced signal. Other performance metrics of interest for such a

transducer are the conversion efficiency, η_{OM} , and bandwidth, γ_m . In continuous-wave operation, the conversion efficiency is given by $\eta_{OM} = \frac{\gamma_{OM}}{\gamma_{OM} + \gamma_0 + \gamma_p}$. We calibrate γ_{OM} for different n_c using electromagnetically induced transparency [18] [see Supplement 1, Fig. S3(a) for details]. Due to the low γ_0 in our devices, we expect high conversion efficiency for modest values of n_c . Specifically, operation at $n_c \approx 13$ and 3 is expected to yield $\eta_{OM} \approx 50\%$ in devices I and II, respectively. The bandwidth of the transducer is limited by the total acoustic linewidth, which is dominated by the optomechanical backaction $\gamma_m \approx \gamma_{OM}$ in the regime of high conversion efficiency.

To characterize the transducer-added noise under continuous-wave laser excitation, we use the measurement setup shown schematically in Fig. 3(a), where we perform single-photon counting at the optical cavity resonance frequency. The data in Figs. 3(b) and 3(c) show n_{th} measured with varying n_c for devices I and II, respectively. In the high-power regime, specifically for $n_c > 500$, the n_{th} data has been corrected for the limited bandwidth of the sideband filter when the acoustic bandwidth γ_m starts to approach the sideband filter linewidth (see Supplement 1, Section 3 for details). The top x -axis displays the corresponding γ_{OM} for side-coupled devices. The green and purple curves in these panels show results from similar measurements of thermal occupancy of the acoustic mode performed previously on 1D-OMCs [3] and butt-coupled 2D-OMCs [11]. We observe that side-coupled 2D-OMCs allow for lower thermal noise across a wide range of input optical powers. A minimum n_{th} of 0.28 ± 0.01 is achieved for device I at $n_c = 2030$, corresponding to an optomechanical transduction efficiency of $98.6 \pm 0.2\%$, and a bandwidth of $\gamma_{OM}/2\pi \approx 6$ MHz.

We model the thermal occupancy n_{th} using the heating model introduced in the previous section. However, in contrast with the measurements with $\Delta = 0$ in the previous section, the majority of the incident power is reflected under detuned operation with $\Delta = -\Omega_m$, and parasitic optical absorption in the coupling waveguide can contribute substantially to the hot bath. To include this

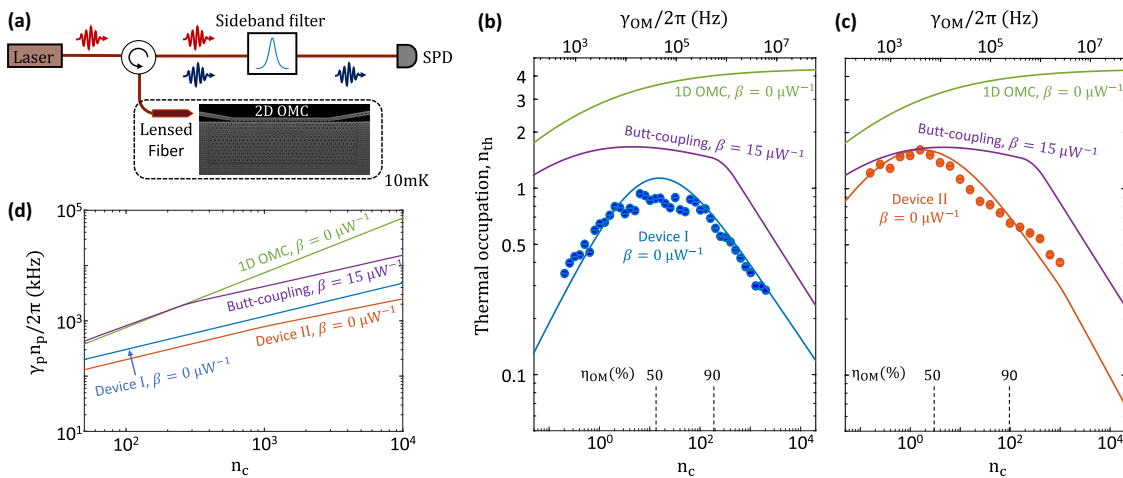


Fig. 3. Phonon-to-photon transduction under continuous-wave excitation. (a) Schematic of measurement setup showing single-photon counting of up-converted photons at the optical resonance frequency with the OMC pumped continuously on the red-detuned sideband ($\Delta = -\Omega_m$) of the optical resonance. Measured thermal phonon occupancy, n_{th} , with varying optical power, shown on the bottom x -axis in units of intra-cavity photon occupation, n_c , and on the top-axis in units of optomechanical transduction rate, γ_{OM} . Results are shown on separate charts for (b) device I, and (c) device II. Filled circles are data points whereas the solid line indicated with $\beta = 0 \mu W^{-1}$ is the modeled n_{th} dependence using Eq. (2). For comparison, model curves are shown for a butt-coupled 2D-OMC ($\beta = 15 \mu W^{-1}$) [11], and 1D-OMC [3]. Dashed lines indicate the n_c value for optomechanical transduction efficiency $\eta_{OM} = 50\%$ and 90% . For $n_c = 1$, on-chip input powers for devices I and II are $P_{in} = 0.20 \mu W$ and $0.28 \mu W$, respectively. (d) Estimated heating rate of the acoustic resonator $\gamma_p n_p / 2\pi$ as a function of n_c under $\Delta = -\Omega_m$ for different devices plotted for their measured value of β .

effect in our heating model, we define an effective photon occupation associated with the coupling waveguide, n_{wg} , varying linearly with the input power as $n_{wg} = \beta P_{in}$ for some fixed constant, β , and the input power, P_{in} . We then add the contributions from both cavity and waveguide components and define the parameters of the modified hot bath as $n_p[n_c, \beta] \rightarrow n_p[n_c + \beta P_{in}]$, and similarly for γ_p . The thermal occupation of the acoustic mode is then given by

$$n_{th} = \frac{\gamma_p[n_c, \beta]n_p[n_c, \beta] + \gamma_0 n_f}{\gamma_p[n_c, \beta] + \gamma_0 + \gamma_{OM}[n_c]}. \quad (2)$$

For small n_c , Eq. (2) is dominated by heating from the hot bath $\gamma_p n_p$ and exhibits an increase in n_{th} with increasing n_c . Conversely for large n_c , n_{th} decreases with increasing n_c as a consequence of backaction cooling γ_{OM} . The turnaround point between these two regimes is influenced by parasitic optical absorption in the coupling waveguide. For example, the solid blue and orange curves in Figs. 3(b) and 3(c) show the predicted thermal phonon occupancy if the waveguide-heating contribution, β , were set to zero. We see that the experimental data from both devices I and II is in reasonable agreement with the $\beta = 0$ curves. This indicates that waveguide-related heating is negligible in side-coupled 2D-OMC geometry. In comparison, for the butt-coupled 2D-OMCs, β was measured to be $15 \mu\text{W}^{-1}$ [11].

While n_{th} in Eq. (2) depends on the optomechanical device parameters γ_0 and γ_{OM} , improvements purely based on geometric modifications of the device platform under detuned operation $\Delta = -\Omega_m$ can be studied using the heating rate $\gamma_p n_p / 2\pi [n_c, \beta]$, and is plotted in Fig. 3(d) for various devices. For 1D-OMC, the heating rate scales linearly ($\gamma_p n_p \propto n_c$), similar to the cooling rate ($\gamma_{OM} \propto n_c$), which results in the saturation of n_{th} to a few phonon levels as n_c increases. 2D geometries are expected to have a lower magnitude of the heating rate due to larger thermal contact with the cold bath. However, due to a large $\beta = 15 \mu\text{W}^{-1}$, the butt-coupling design exhibits almost identical heating performance ($\gamma_p n_p \propto n_c^{0.9}$) to that of 1D-OMC for $n_c < 300$, and only becomes sublinear for $n_c > 300$ ($\gamma_p n_p \propto n_c^{0.6}$). In contrast, for side-coupled geometries, the heating rate scales sub-linearly ($\gamma_p n_p \propto n_c^{0.6}$) for all n_c range measured and has a lower magnitude. Specifically, for device II, the heating rate is reduced by approximately six-fold compared to the butt-coupling design for $n_c > 300$.

5. PHONON-TO-PHOTON TRANSDUCTION UNDER PULSED LASER EXCITATION

Pulsed transduction schemes are often preferred due to the delayed heating response of the acoustic resonator [9], which allows for the initialization of the optomechanical transduction pulse prior to the onset of heating. We characterize the performance of side-coupled 2D-OMC as a transducer in pulsed mode by sending short rectangular pulses on the red sideband. A pulse duration of $\tau_d = 500$ ns is selected to account for the finite rise time of the sideband filters (≈ 200 ns). The transduction efficiency in the pulsed mode is given by

$$\eta_{OM} = \frac{\gamma_{OM}}{\gamma_{OM} + \gamma_0 + \gamma_p} \left(1 - e^{-(\gamma_0 + \gamma_p + \gamma_{OM})\tau_d}\right). \quad (3)$$

Figure 4 shows the internal transduction noise \bar{n} for device II in a pulsed scheme along with similar measurements performed previously using 1D-OMC [3] and butt-coupling design [11] at $n_c = 10$. The n_c value corresponding to the optomechanical conversion efficiency $\eta_{OM} = 10\%$, 50% , and 90% for device II, are indicated

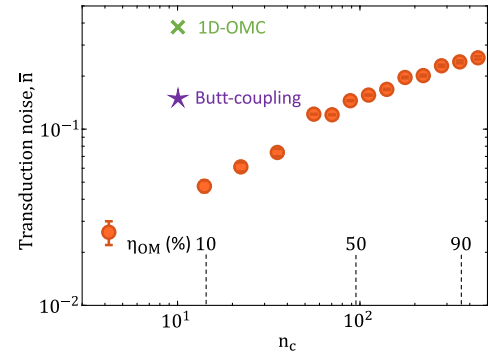


Fig. 4. Phonon-to-photon transduction under pulsed laser excitation. Internal added noise, \bar{n} (red data points), as a function of the peak intracavity pump photon number, n_c . All noise measurements are performed on device II with rectangular optical pump pulses with a pulse width of 500 ns at a repetition rate of 250 Hz. For comparison, \bar{n} is shown for butt-coupling design [11], and 1D-OMC [3]. Dashed lines indicate the n_c value for transduction efficiency $\eta_{OM} = 10\%$, 50% , and 90% for device II. For $n_c = 1$, on-chip input power is $P_{in} = 0.28 \mu\text{W}$.

with dashed lines. Given the low intrinsic linewidth of the acoustic resonator for this device ($\gamma_0/2\pi = 0.97$ kHz), we used a repetition rate of 250 Hz to allow the acoustic mode to sufficiently thermalize to the cold bath between successive optical pulses. For the highest optical power we could send to the device ($n_c = 444$), we measured $\bar{n} = 0.25 \pm 0.01$, which corresponds to a transduction efficiency of $\eta_{OM} = 93.1 \pm 0.8\%$. This constitutes a significant enhancement across transduction metrics over 1D-OMC with $(n_c, \bar{n}, \eta_{OM}) \simeq (10, 0.4, 4\%)$ [3].

6. DISCUSSION

The side-coupled 2D-OMC design presented here reduces optical-absorption-induced thermal noise in OMCs, a major obstacle in quantum application requiring operation at millikelvin temperatures. We anticipate that further reduction in thermal noise can be achieved through surface passivation techniques [19], potentially minimizing optical absorption via surface defect reduction.

This result unlocks new possibilities for more quantum-coherent applications using OMCs. The compact form factor and long-lived acoustic mode of such devices are attractive for applications such as quantum memory for telecom photons [4]. While we achieved a low intrinsic decay rate of 0.97 kHz for the acoustic resonator, we anticipate that embedding the 2D-OMC in a cross phononic shield may lead to drastically lower intrinsic decay rates [3,11]. The low thermal occupation of the acoustic resonator presents an opportunity to investigate two-level systems (TLS) in amorphous solids [3,20,21], further expanding the potential of OMCs in quantum technologies.

The improved performance of our side-coupled 2D-OMC design in pulsed operation promises significant advancements in single-photon heralding and remote entanglement generation. For a realistic pulse repetition rate of 10 kHz and a total detection efficiency of 5%, we estimate a single-photon heralding rate of 465 Hz, a substantial increase compared to the 20 Hz achievable with 1D-OMCs. Furthermore, in a two-node remote entanglement experiment, we project a photon coincidence rate of 21 Hz, representing a ~ 500 -fold enhancement over the 0.04 Hz rate achievable with 1D-OMCs.

In the context of microwave-to-optical quantum transduction, side-coupled 2D-OMC could be integrated into piezo-optomechanical transducers by designing a piezo-acoustic cavity that couples the electrical circuit to the optomechanical circuit through a phononic waveguide [5]. Such transducers offer the potential for large-bandwidth, low-noise, and near-unity efficiency conversion between microwave and optical signals. While this study has focused on improved thermal handling in silicon-based devices, piezo-optomechanical transducers utilize heterogeneously integrated platforms with optically robust microwave resonators [6–8], potentially involving distinct heating mechanisms. Nevertheless, our findings establish a performance benchmark for microwave-to-optical transduction. By connecting such a transducer to an off-chip qubit module [22–24], high optical powers can be employed without compromising superconducting qubit coherence. Additionally, techniques like atomic force microscope (AFM) nano-oxidation can be used to precisely match frequencies between remote piezo-optomechanical systems [25], paving the way for optically mediated remote entanglement of superconducting qubit nodes.

Funding. Amazon Web Services; National Science Foundation (PHY-1125565); Army Research Office (W911NF-18-1-0103); U.S. Department of Energy Office of Science National Quantum Information Science Research Centers (Q-NEXT, DE-AC02-06CH11357); Institute for Quantum Information and Matter (IQIM); Gordon and Betty Moore Foundation; Kavli Nanoscience Institute at Caltech; AWS Center for Quantum Computing.

Acknowledgment. The authors thank Matthew Shaw and Boris Korzh for providing single photon detectors in this work. We thank Piero Chiappina for helpful discussions. S.M. acknowledges support from the IQIM Postdoctoral Fellowship. Amazon Web Services (AWS) provided partial funding support for this work through a sponsored research grant.

Disclosures. O.P. is currently employed by AWS as Director of their quantum hardware program.

Data availability. Data underlying the results presented in this paper are not publicly available at this time but may be obtained from the corresponding author upon reasonable request.

Supplemental document. See Supplement 1 for supporting content.

REFERENCES

1. M. Eichenfield, C. P. Michael, R. Perahia, *et al.*, “Actuation of micro-optomechanical systems via cavity-enhanced optical dipole forces,” *Nat. Photonics* **1**, 416–422 (2007).
2. J. Chan, A. H. Safavi-Naeini, J. T. Hill, *et al.*, “Optimized optomechanical crystal cavity with acoustic radiation shield,” *Appl. Phys. Lett.* **101**, 081115 (2012).
3. G. S. MacCabe, H. Ren, J. Luo, *et al.*, “Nano-acoustic resonator with ultralong phonon lifetime,” *Science* **370**, 840–843 (2020).
4. A. Wallucks, I. Marinković, B. Hensen, *et al.*, “A quantum memory at telecom wavelengths,” *Nat. Phys.* **16**, 772–777 (2020).
5. M. Mirhosseini, A. Sipahigil, M. Kalaei, *et al.*, “Superconducting qubit to optical photon transduction,” *Nature* **588**, 599–603 (2020).
6. S. Meesala, S. Wood, D. Lake, *et al.*, “Non-classical microwave–optical photon pair generation with a chip-scale transducer,” *Nat. Phys.* **20**, 871–877 (2024).
7. W. Jiang, F. M. Mayor, S. Malik, *et al.*, “Optically heralded microwave photon addition,” *Nat. Phys.* **19**, 1423–1428 (2023).
8. M. J. Weaver, P. Duivestijn, A. C. Bernasconi, *et al.*, “An integrated microwave-to-optics interface for scalable quantum computing,” *Nat. Nanotechnol.* **19**, 166–172 (2023).
9. S. M. Meenehan, J. D. Cohen, G. S. MacCabe, *et al.*, “Pulsed excitation dynamics of an optomechanical crystal resonator near its quantum ground state of motion,” *Phys. Rev. X* **5**, 041002 (2015).
10. A. H. Safavi-Naeini, J. T. Hill, S. Meenehan, *et al.*, “Two-dimensional phononic-photon band gap optomechanical crystal cavity,” *Phys. Rev. Lett.* **112**, 153603 (2014).
11. H. Ren, M. H. Matheny, G. S. MacCabe, *et al.*, “Two-dimensional optomechanical crystal cavity with high quantum cooperativity,” *Nat. Commun.* **11**, 1–10 (2020).
12. G. Madiot, M. Albrechtsen, S. Stobbe, *et al.*, “Multimode optomechanics with a two-dimensional optomechanical crystal,” *APL Photonics* **8**, 116107 (2023).
13. R. G. Povey, M.-H. Chou, G. Andersson, *et al.*, “Two-dimensional optomechanical crystal resonator in gallium arsenide,” *Phys. Rev. Appl.* **21**, 014015 (2024).
14. A. H. Safavi-Naeini and O. Painter, “Proposal for an optomechanical traveling wave phonon-photon translator,” *New J. Phys.* **13**, 013017 (2011).
15. N. Zen, T. A. Puurtinen, T. J. Isotalo, *et al.*, “Engineering thermal conductance using a two-dimensional phononic crystal,” *Nat. Commun.* **5**, 3435 (2014).
16. J. Maire, R. Anufriev, R. Yanagisawa, *et al.*, “Heat conduction tuning by wave nature of phonons,” *Sci. Adv.* **3**, e1700027 (2017).
17. M. R. Wagner, B. Graczykowski, J. S. Reparaz, *et al.*, “Two-dimensional phononic crystals: Disorder matters,” *Nano Lett.* **16**, 5661–5668 (2016).
18. A. H. Safavi-Naeini, T. M. Alegre, J. Chan, *et al.*, “Electromagnetically induced transparency and slow light with optomechanics,” *Nature* **472**, 69–73 (2011).
19. M. Borselli, T. J. Johnson, and O. Painter, “Measuring the role of surface chemistry in silicon microphotonic,” *Appl. Phys. Lett.* **88**, 131114 (2006).
20. M. Chen, J. C. Owens, H. Putterman, *et al.*, “Phonon engineering of atomic-scale defects in superconducting quantum circuits,” *Sci. Adv.* **10**, eado6240 (2024).
21. A. Y. Cleland, E. A. Wollack, and A. H. Safavi-Naeini, “Studying phonon coherence with a quantum sensor,” *arXiv* (2023).
22. R. Delaney, M. Urmey, S. Mittal, *et al.*, “Superconducting-qubit readout via low-backaction electro-optic transduction,” *Nature* **606**, 489–493 (2022).
23. T. van Thiel, M. Weaver, F. Berto, *et al.*, “High-fidelity optical readout of a superconducting qubit using a scalable piezo-optomechanical transducer,” *arXiv* (2023).
24. G. Arnold, T. Werner, R. Sahu, *et al.*, “All-optical single-shot readout of a superconducting qubit,” *arXiv* (2023).
25. U. Hatipoglu, S. Sonar, D. P. Lake, *et al.*, “In situ tuning of optomechanical crystals with nano-oxidation,” *Optica* **11**, 371–375 (2024).